Available online at www.sciencedirect.com
ScienceDirect
Trans. Nonferrous Met. Soc. China 35(2025) 2830−2845
Transactions of Nonferrous Metals Society of China
www.tnmsc.cn

Role of cryorolling in enhancing corrosion resistance of Al−Mg−Mn−Sc alloy sheets

Hao GU[1,2], Shuai-guang JIA[1,2], Zhi-de LI[3], Hai-tao GAO[1,2,3], Zheng-yu WANG[4], Charlie KONG[5], Hai-liang YU[1,2,3]

1. State Key Laboratory of Precision Manufacturing for Extreme Service Performance, Central South University, Changsha 410083, China;
2. College of Mechanical and Electrical Engineering, Central South University, Changsha 410083, China;
3. Light Alloys Research Institute, Central South University, Changsha 410083, China;
4. Shimadzu (China) Co., Ltd., Shanghai 200233, China;
5. Electron Microscope Unit, University of New South Wales, Sydney, NSW 2052, Australia

Received 10 January 2024; accepted 1 July 2024

Abstract: The service performance of Al alloy sheets can be improved by controlling the rolling temperature. In this study, the corrosion resistance of Al−Mg−Mn−Sc alloy sheets was enhanced through cryorolling (CR). The corrosion resistance of the CR samples with 50% rolling reduction was superior to that of the room-temperature rolled (RTR) samples. After the sensitization treatment (ST), the maximum intergranular corrosion (IGC) depth for the CR samples was 35.2 μm, while it was 53.9 μm for the RTR samples. Similarly, the mass losses were 56.89 and 73.11 mg/cm^2 for the CR and RTR samples after ST, respectively. In addition, the impedance modulus of the CR sample was more than twice that of the RTR sample. Superior pitting resistance can be attributed to the thicker passivation film and the Al_6(Mn,Fe) phases being broken and interspersed in CR samples. Furthermore, the sub-grains, shear bands, dispersive Al_3(Sc,Zr) phases, fewer high-angle grain boundaries and high-density dislocations in the CR samples impeded the continuous precipitation of the β (Al_3Mg_2) phase along grain boundaries while promoting its formation inside grains instead. These microscopic characteristics significantly reduced the electrical coupling effect between β phase and the Al matrix, leading to a considerable decrease in IGC occurrence.

Key words: Al−Mg−Mn−Sc alloy; cryorolling; corrosion resistance; microstructure; grain size; secondary phase

1 Introduction

The Al−Mg alloys are a series of non-heat treatment strengthened alloys, which exhibit excellent fatigue performance, welding performance, and resistance to corrosion in marine and atmospheric environments [1]. However, prolonged exposure of Al−Mg alloys to high temperatures (323−473 K) causes the Mg element to separate from the solid solution and diffuse to the grain boundaries (GBs), thus generating β (Al_3Mg_2) phase precipitates [2]. The corrosion potential of β phase is lower than that of the Al matrix, allowing β phase to establish a tiny battery loop with the surrounding Al matrix. To prevent the corrosion of the cathode Al matrix, the anode β phase at the GB is sacrificed [3], which considerably increases the intergranular corrosion (IGC) sensitivity of the alloy. If β phase continuously accumulates at GBs, the corrosion will progress into continuous IGC [4]. This occurrence is referred to as “sensitization”. When IGC occurs within a crystal lattice, it reduces strength at the GBs, ultimately leading to fracture failure.

Corresponding author: Hai-liang YU, Tel/Fax: +86-731-88879351, E-mail: yuhailiang@csu.edu.cn
https://doi.org/10.1016/S1003-6326(25)66851-8

The sensitivity of the IGC is influenced by several factors, such as the Mg content [5], misorientation of the GBs [6−8], the secondary phase [9,10], and dislocation [11]. These factors impact the position, continuity, and shape of β phase precipitates [12,13]. Studies [12,14,15] have verified that incorporating small amounts of rare earth elements, like Sc, significantly inhibits the recrystallization and enhances the mechanical properties and corrosion resistance of Al−Mg alloys. Furthermore, the IGC resistance of the AA5182 sheet may be improved by adding Sc and Zr elements [12]. This is because the presence of Al_3(Sc,Zr) phases inhibits the recrystallization and the sub-grains prevent the continuous precipitation of β phase at the GBs. According to PAN et al [16], the addition of the Sc element increased the percentage of the low-angle grain boundaries (LAGBs) and reduced the diffusion channel of the Mg element to high-angle grain boundaries (HAGBs). As a result, the IGC performance is improved as the breadth of β phase gets smaller and more discontinuous. However, alloying has its limitations in solving the local corrosion. It is still widely concerned research to improve the corrosion resistance of Al−Mg alloy.

The rolling process is widely used in the preparation of the Al−Mg alloy sheets. The influence of rolling temperature on the microstructure of the alloy is posited to exert subsequent ramifications on the properties of the material [17], encompassing the corrosion properties. Compared with room-temperature rolling (RTR), cryorolling (CR) can effectively enhance the properties of pure metals [18,19], alloys [20−22], and composite materials [23]. The CR Al alloys showed outstanding resistance to corrosion. KUMAR et al [24] discovered that the CR AA6082 samples had a higher corrosion potential and pitting potential than the RTR samples. This finding was explained by the higher dislocation density and dissolution of the $Mg_4Al_3Si_4$ phases in the Al matrix, which formed a passive film. GOPALA KRISHNA et al [25] reported that the Al−4Zn−2Mg alloy samples subjected to CR and peak aging exhibited a higher corrosion potential and a lower corrosion current density than the coarse-grain samples. This was attributed to the absence of the coarse $MgZn_2$ phase at the GBs and sub-grain hindrance to the anode phase precipitation. The corrosion current density of the CR + peak-aged AA2024 samples was likewise significantly lower than that of the solution heat treatment + aged samples [26]. SINGH et al [27] suggested that the coarse secondary phase caused the pitting of AA5083. They found that both the samples subjected to the CR and CR + annealing at 573 K for 5 min exhibited superior corrosion resistance compared to the solution-treated samples. It is attributed to the high density of dislocations and grain boundaries contributing to the formation of passive films. However, the effect of CR on the precipitation of β phase was not investigated. The above studies indicate that the CR affects the corrosion properties of the Al alloy. In addition, upon the occurrence of rolling deformation in the alloy, there is a concomitant escalation in the density of dislocations and the generation of internal stresses. This phenomenon leads to an instability of the microstructure, which is manifested as a decrease in the corrosion resistance of the material. Therefore, stable annealing is required for rolled alloys. TANG et al [28] and FANG et al [29] found that the optimal mechanical properties and corrosion resistance of the RTR Al−Mg−Mn−Sc−Zr alloy can be achieved after annealing at 573 K for 1 h.

In previous studies [18,20], it was discovered that CR enhances the strength and high-temperature plasticity of 5xxx Al alloy. These studies belong to the basic research included in the systematic research of CR. At present, there is no available report regarding the evolution of β phase precipitation in CR Al−Mg−Mn−Sc alloy. Moreover, studies are scarce on the effect of CR on the corrosion resistance of the Al−Mg−Mn−Sc alloys. This work aims to fill the literature gap in the comparison of corrosion properties of the RTR and CR Al−Mg−Mn−Sc alloys. The microstructure design of Al−Mg−Mn−Sc alloys resistant to pitting and IGC was achieved by introducing more dislocations, LAGBs, sub-grains, and shear bands through CR. The findings indicated that the CR Al−Mg−Mn−Sc alloy sheets exhibited superior corrosion resistance. Ultimately, the corrosion mechanism of the CR samples was clarified. This work provided a theoretical basis for enhancing the corrosion properties of Al−Mg−Mn−Sc alloy sheets and supports the application of these alloys in the field of engineering.

2 Experimental

The Al−Mg−Mn−Sc alloy was cast using pure aluminum (99.9%) and intermediate alloys such as Al−38Mg (wt.%), Al−2Sc (wt.%), Al−20Mn (wt.%), and Mg−25Zr (wt.%). The melting temperature ranged from 993 to 1053 K. The molten aluminum underwent degassing and slag removal by adding a refining agent. It was then stirred at 993 K for 1 h before being placed into the cast iron mold. The element contents obtained by the Spectro Blue plasma emission spectrometer are presented in Table 1. The ingot underwent homogenized treatment at 733 K for 12 h in a muffle furnace [28], followed by hot rolling (HR) at 723 K, reducing the thickness of the ingot from 30 to 6 mm. Subsequently, the sheets were annealed at 573 K for 1 h and then used as raw material (RM).

Table 1 Chemical composition of Al−Mg−Mn−Sc alloy sheets (wt. %)

Mg	Mn	Fe	Si	Sc	Zr	Al
4.28	0.44	0.04	0.05	0.25	0.09	Bal.

Subsequently, the RM sheets were processed using CR and RTR on a four-high rolling mill with a work roll diameter of 320 mm. The line speed was 4 m/min, and a thickness reduction of 0.2 mm per pass was performed until the sheets reached a thickness of 3 mm. Prior to CR, the sheets were cooled using liquid nitrogen in an incubator for 30 min for the initial pass and cooled in liquid nitrogen for 5 min before the subsequent CR passes. After CR and RTR, the sheets were annealed in a muffle furnace at 573 K for 1 h [28,29], which were defined as CR+A and RTR+A, respectively. The sensitization treatment (ST) involved holding the CR and RTR sheets inside a constant temperature blast drying oven at 433 K for 100 h to simulate the prolonged high-temperature service conditions and precipitate β phases (defined as CR+ST and RTR+ST), respectively.

The Barker reagent (5 mL H_2O and 200 mL HBF_4) was prepared for anode coating. The polarizing module of optical microscopy (OM) was used for observation. The anode coating process involved applying a power supply voltage of 25 V, a current density ranging from 0.1 to 0.3 A/cm^2, and a working time from 40 to 80 s. The grain size was estimated by measuring the width of the elongated grains. The electron backscatter diffraction (EBSD) analysis was performed to study the microstructures of the samples along the rolling direction (RD)−normal direction (ND) plane using a Thermo Fisher Helios 5 CX scanning electron microscope (SEM). The samples were prepared with the HITACHI IM4000 Plus ion milling equipment. The microstructures of the Al−Mg−Mn−Sc alloy were analyzed using the Talos F200X and Tecnai G2 F20 transmission electron microscope (TEM) on two planes: the RD−ND plane and the RD−transverse direction (TD) plane. The TEM samples were prepared using the Thermo Fisher Helios G4 PFIB instruments. A fast Fourier transform (FFT) analysis was conducted by Digital Micrograph software to process the high-resolution TEM (HRTEM) images.

The IGC sensitivity of the Al−Mg−Mn−Sc alloy was evaluated by IGC immersion tests following GB/T 7998—2005 (ASTM G110—1992). Prior to testing, the samples were cleaned using a 100 g/L NaOH solution for 5 min followed by HNO_3 (30 vol.%) solution for 2 min. Following the washing process with distilled water, the samples were submerged in the IGC solution (30 g NaCl, 10 mL HCl, and 1 L distilled water) at (308±2) K for 24 h. The RD−ND planes of samples were examined using OM to determine the maximum corrosion depth.

The nitric acid mass loss test (NAMLT) was conducted following the guidelines outlined in GB/T 26491—2011 (ASTM G67). The sample with dimensions of 50 mm (RD) × 6 mm (TD) × 2.5 mm (ND) was polished and treated with a 50 g/L NaOH solution at 353 K for 1 min. Afterward, the sample was immersed in a HNO_3 solution (500 mL HNO_3 + 500 mL distilled water) for 30 s. Finally, the sample was immersed in concentrated nitric acid solution (600 mL HNO_3 + 400 mL distilled water) at 303 K for 24 h. The mass loss per unit area was calculated to determine the IGC sensitivity of the alloy. The test was repeated three times.

The CR and RTR samples underwent the ST at 433 K for 48 and 100 h, respectively. The Adminal electrochemical workstation and 3.5 wt.% NaCl solution were utilized for electrochemical experiments. A three-electrode cell comprising the test samples served as the working electrode, a platinum plate electrode served as the counter electrode, and a saturated calomel electrode (SCE)

served as the reference electrode during the experiment. The potentiodynamic polarization tests were conducted with a scan rate of 3 mV/s, covering a range from −500 to 500 mV relative to the open circuit potential. Electrochemical impedance spectroscopy (EIS) was performed within the frequency range from 100 mHz to 100 kHz, with an amplitude of ±5 mV. The Zahner Analysis software was utilized to analyze the results.

3 Results

3.1 Microstructure evolution of Al−Mg−Mn−Sc sheets

Figure 1 displays the OM images and the average grain sizes of the RM, CR, RTR, CR+A, and RTR+A samples. The grain width along the ND is counted as the grain size. The size of more than 100 grains was measured for each sample and their average value was taken as the average grain size of the sample. Figure 1(b) shows that the grains of RM samples can be characterized as diamond or oval shape, with an average grain size of (22.3±7.8) μm. The grains were elongated along the RD after rolling. As shown in Fig. 1(c), the average grain size of the CR sample was greatly reduced to (4.3±2.0) μm. The average grain size of the CR+A sample increased to (5.8±2.7) μm (Fig. 1(e)). Compared with CR and CR+A samples, the average grain sizes of RTR and RTR+A samples were larger, which were (6.7±2.5) and (8.3±3.3) μm, as seen in Figs. 1(d) and (f), respectively. Besides, the CR and CR+A samples exhibited universal shear bands.

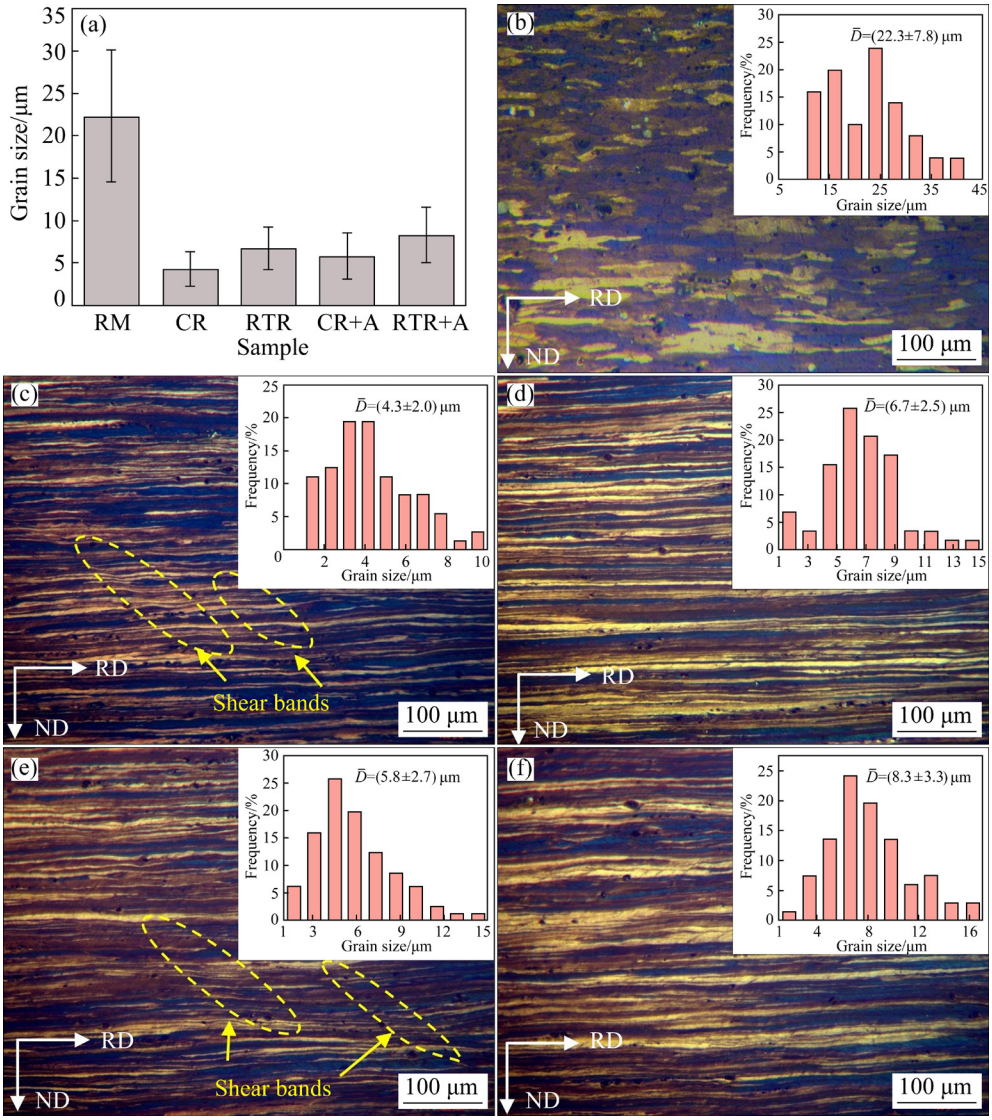

Fig. 1 Average grain size and OM images of Al−Mg−Mn−Sc alloy sheets: (a) Average grain size of different samples; OM images of RM (b), CR (c), RTR (d), CR+A (e), and RTR + A (f) samples

The inverse pole figure (IPF) maps of CR+A and RTR+A samples are depicted in Figs. 2(a) and (d), respectively. A recrystallized grain is defined as one having an average directional stretch of less than 2. According to the grain orientation spread (GOS) maps (Figs. 2(b) and (e)), the proportion of recrystallized grains in the CR+A samples (10.84%) was lower than that in the RTR+A samples (14.24%). The orientation difference between adjacent grains is defined as θ. θ>15° was defined as HAGBs and 2°<θ<15° was defined as LAGBs. The GB distribution maps (Figs. 2(c) and (f)) revealed that HAGBs occupied 33.4% in the CR+A sample and 45.4% in the RTR+A sample.

Figure 3 presents the TEM image and the corresponding EDS mappings of the RM sample.

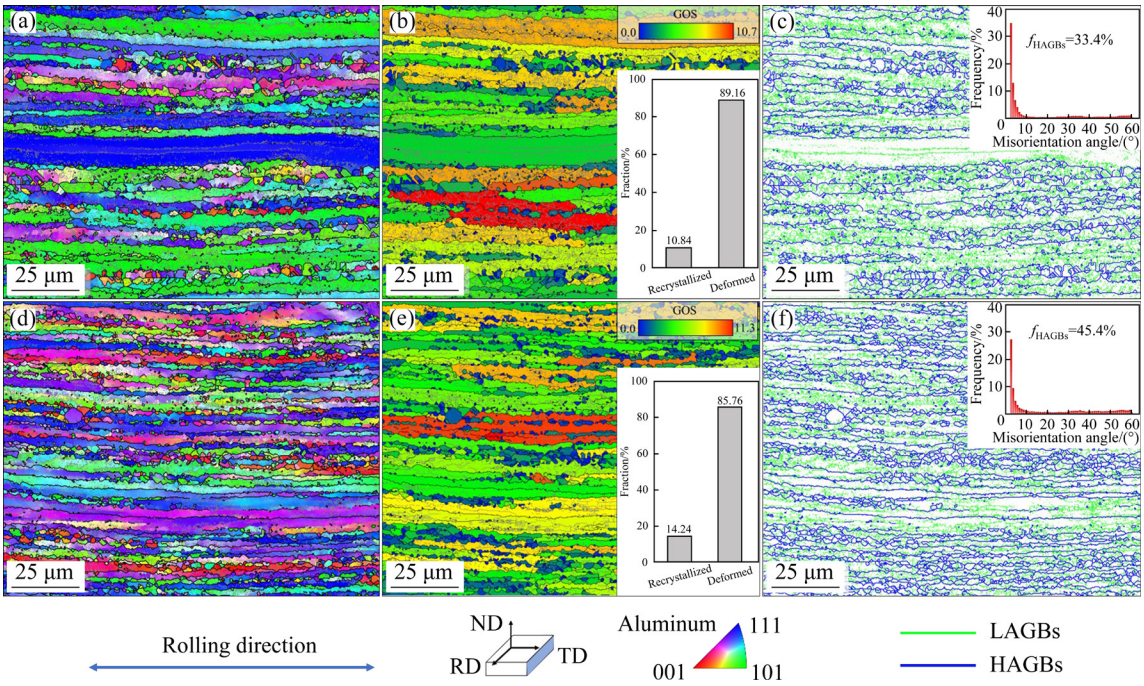

Fig. 2 EBSD images of CR+A (a, b, c) and RTR+A (d, e, f) samples: (a, d) IPF maps; (b, e) GOS maps; (c, f) GB maps and GB distribution

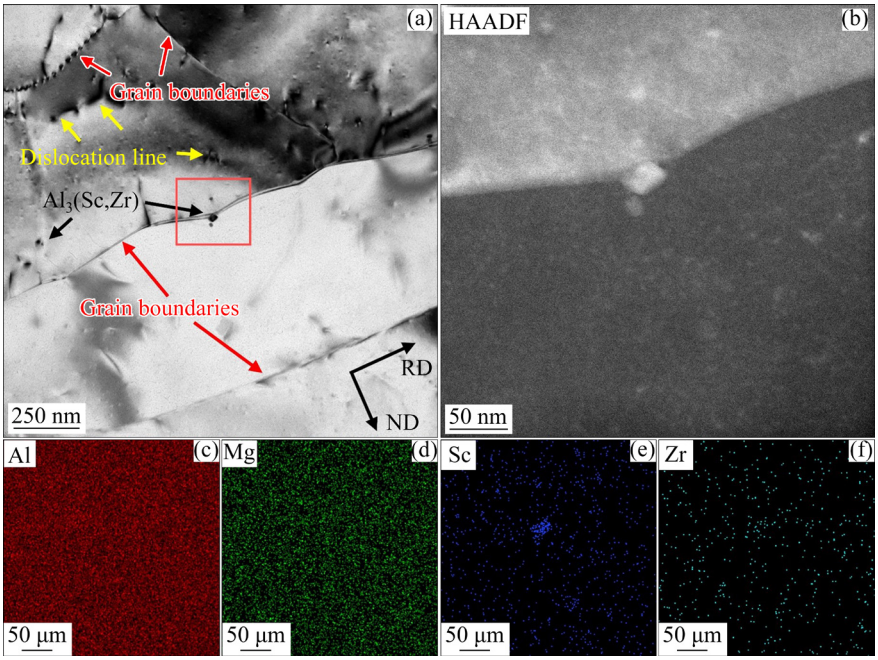

Fig. 3 TEM images of RM sample: (a) Bright field image; (b) HAADF of area depicted inside red box in (a); (c−f) EDS mappings corresponding to (b)

The grains are elongated along RD. The crystal has few dislocation lines and $Al_3(Sc,Zr)$ phases. The EDS mappings revealed that the spherical phase located within the red box corresponded to the $Al_3(Sc,Zr)$ phase.

As shown in Figs. 4(a) and (b), the CR and RTR processes yielded a narrower grain width and a higher quantity of dislocations in comparison to the RM process. The CR sample displayed abundant dislocation tangles. Additionally, $Al_3(Sc,Zr)$ phases were distributed along the RD. The RTR sample exhibited fewer dislocations. The size of $Al_6(Mn,Fe)$ phases in the CR sample is smaller than that in the RTR sample. Figures 4(c) and (d) depict the microstructures of the CR+A and RTR+A samples, respectively. Sub-grains were also detected in these samples. Figure 4(d) shows β phase in the RTR+A sample, which can be observed to appear at the GBs and near the $Al_6(Mn,Fe)$ phase. Similar findings were reported previously as well in Refs. [10,12,13,30]. The TEM results of CR+ST and RTR+ST samples are presented in Figs. 4(e)

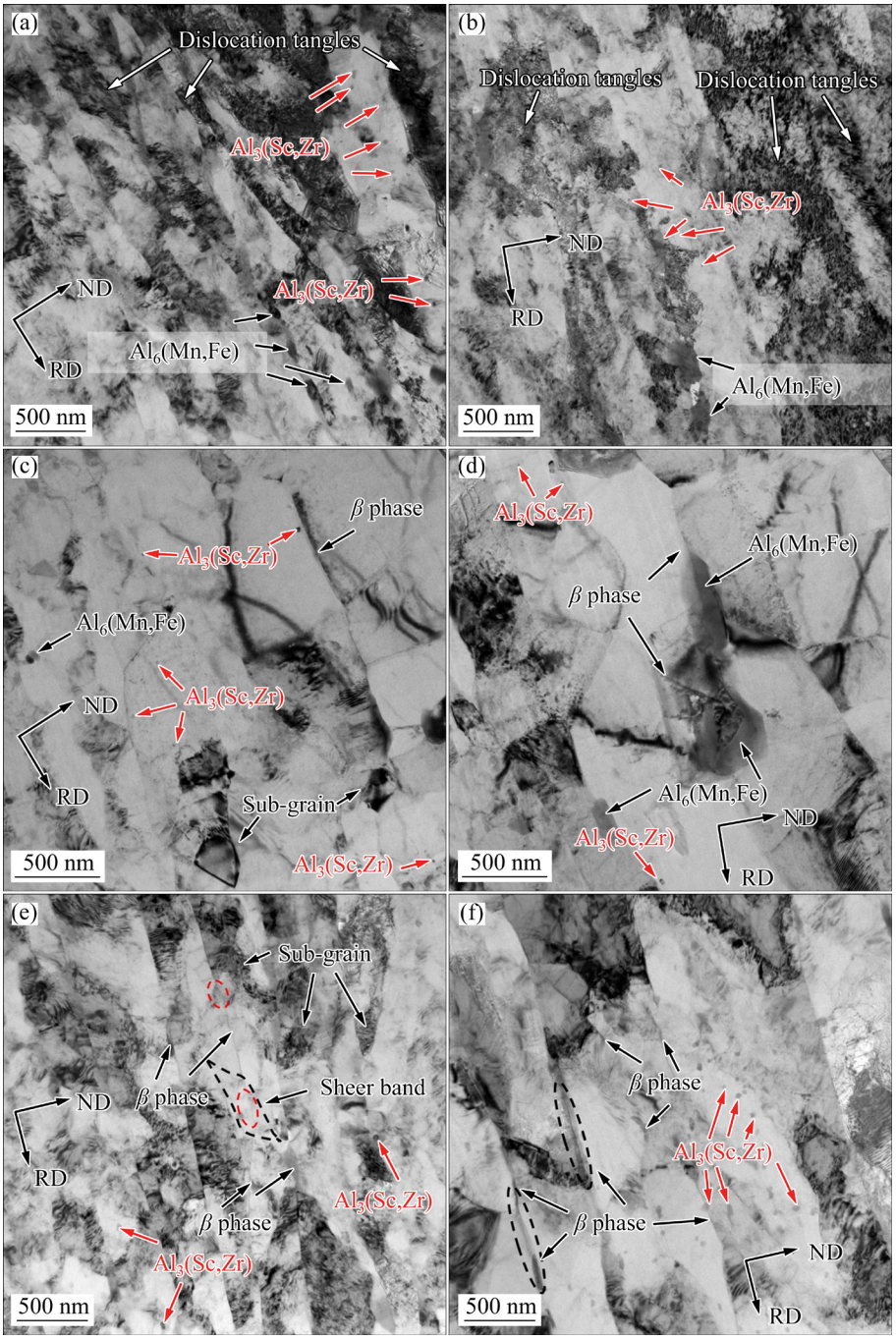

Fig. 4 TEM images of CR (a), RTR (b), CR+A (c), RTR+A (d), CR+ST (e), and RTR+ST (f) samples

and (f), respectively. It was observed that the RTR+ST sample had a broader β phase. The shear bands in the CR+ST sample hindered the precipitation of β phase. The CR+ST sample retained a significant number of dislocations, however, recovery occurred in the RTR+ST sample, which led to a reduction in dislocation density.

3.2 Corrosion properties of Al−Mg−Mn−Sc alloy sheets

After the IGC immersion testing, the RD−ND plane of the Al−Mg−Mn−Sc alloy samples was analyzed and the results are shown in Fig. 5. The rolled and annealed samples exhibited pitting corrosion. Nevertheless, the samples exhibited distinct IGC characteristics after ST. The pitting was mostly observed in the CR and RTR samples, with a maximum pit depth of 9.8 and 21.2 μm, respectively. As is visible in Figs. 5(c) and (d), the annealed samples exhibited both pitting and IGC characteristics. The maximum corrosion depths in the CR+A and RTR+A samples were 15.6 and 21.5 μm, respectively. Significant grain exfoliation took place along the RD, as seen in Figs. 5(e) and (f). The CR+ST and RTR+ST samples reached a maximum IGC depth of 35.2 and 53.9 μm, respectively. The warping of the corrosion surface due to the accumulated corrosion products exerted pressure on the surface grains, leading to the deformation [31].

The IGC sensitivity of the 5xxx Al alloy was assessed using the NAMLT test and the results are shown in Fig. 6. The degree of sensitization (DoS) is attributed mainly to the preferential corrosion of the intergranular β phase and positively correlated with the fraction of β phase volume. According to

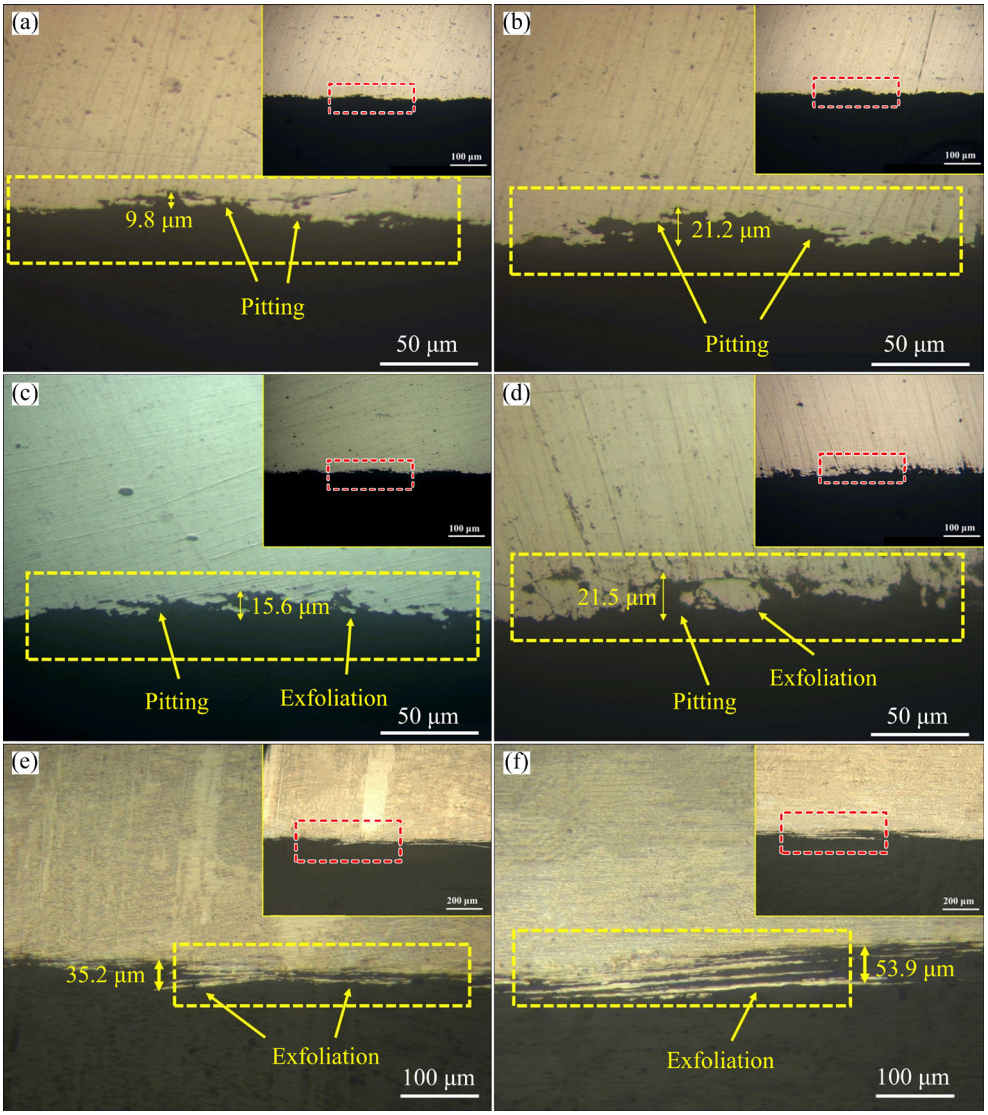

Fig. 5 IGC morphology of CR (a), RTR (b), CR+A (c), RTR+A (d), CR+ST (e), and RTR+ST (f) samples

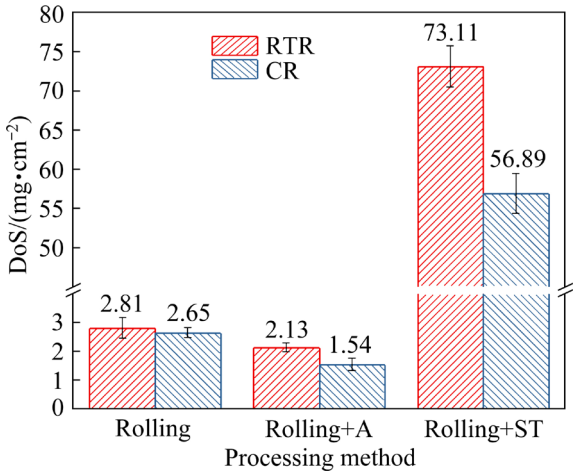

Fig. 6 DoS values of Al−Mg−Mn−Sc alloy obtained through NAMLT test

Ref. [28], a mass loss lower than 15 mg/cm^2 indicates IGC resistance, while a mass loss above 25 mg/cm^2 indicates high sensitivity to IGC. The DoS values obtained for the RTR and CR samples were (2.81±0.36) and (2.65±0.18) mg/cm^2, respectively. These values indicated excellent corrosion resistance according to the established criteria stated above. After annealing at 573 K for 1 h, the DoS values of the RTR+A and CR+A samples decreased to (2.13±0.15) and (1.54±0.22) mg/cm^2, respectively. In order to evaluate the corrosion resistance of the Al−Mg−Mn−Sc alloy sheets during long-term service at high temperatures, the alloy sheets were subjected to 433 K for 100 h to simulate the service conditions. It was observed that the corrosion resistance of the Al−Mg−Mn−Sc alloy decreased significantly after ST, with the DoS values of (73.11±2.63) and (56.89±2.52) mg/cm^2 obtained for the RTR+ST and CR+ST samples, respectively.

Figure 7(a) depicts the potentiodynamic polarization curves of the Al−Mg−Mn−Sc alloy samples. The passivation behavior was seen within the range from −0.90 to −0.25 V, resulting in the formation of a passive film on the surface. The pitting potential (φ_{pit}) is directly proportional to the pitting resistance of the samples. The CR samples exhibited a higher φ_{pit} (−0.197 V) in comparison to the RTR samples. After ST, the φ_{pit} of the RTR samples decreased significantly. The φ_{pit} of the CR+ST(48 h) sample (−0.287 V) was significantly

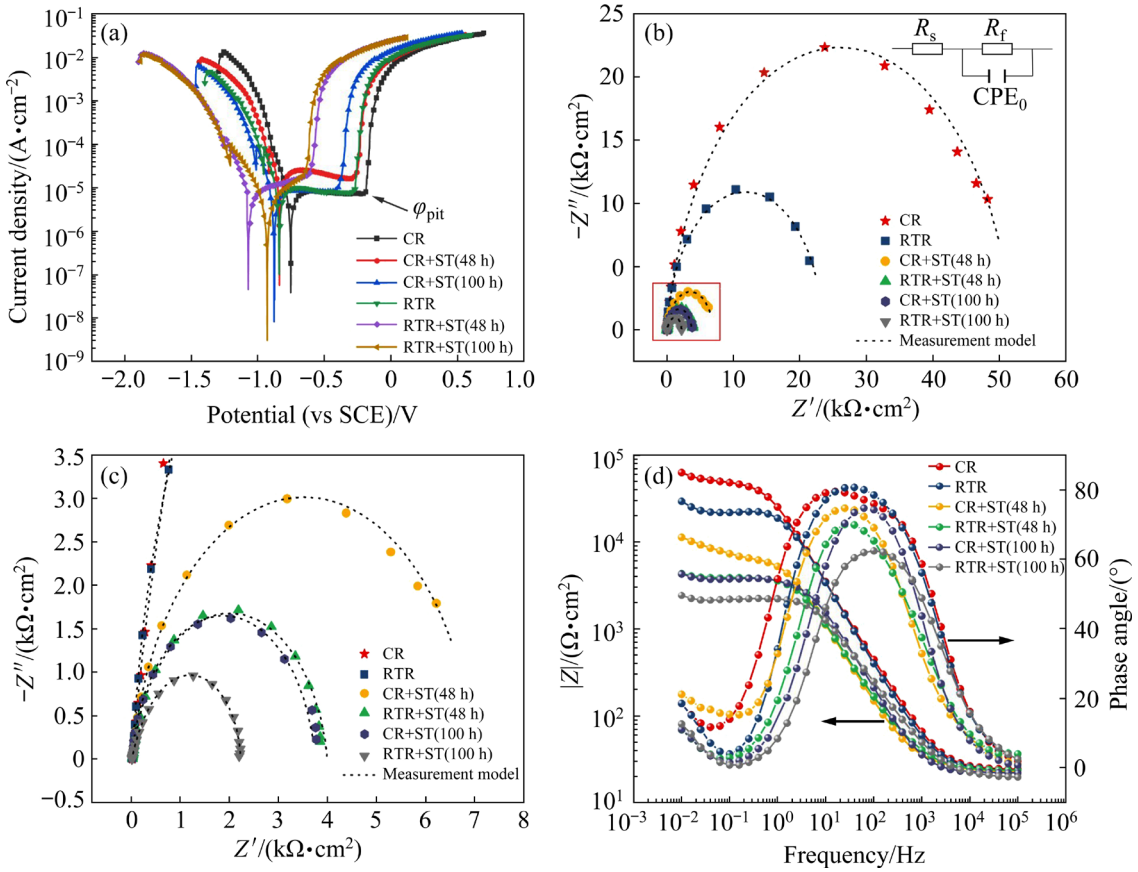

Fig. 7 Results of electrochemical experiments for different samples: (a) Potentiodynamic polarization curves; (b) Nyquist plots and equivalent circuit models; (c) Partial enlargement of (b); (d) Bode plots

higher than that of the RTR+ST (48 h) sample (−0.618 V), suggesting that CR sample has better pitting resistance. Furthermore, the CR sample displayed a corrosion potential (φ_{corr}) of −0.751 V, which was higher than that of the RTR sample (−0.839 V). The φ_{corr} values of the CR+ST(100 h) and RTR+ST(100 h) samples were −0.877 and −0.928 V, respectively. The φ_{corr} decreased by 27.6% in the RTR+ST samples and 16.8% in the CR+ST samples.

The Butler−Volmer equation fit curve obtained using the Zahner Analysis software allowed for the determination of various parameters [14], including the corrosion current density (J_{corr}), anodic Tafel slope (β_a), cathodic Tafel slope (β_c), polarization resistance (R_p), and annual corrosion rate. The values acquired are documented in Table 2. The rolled samples showed the highest R_p, with values of 6.52 kΩ·cm^2 and 4.60 kΩ·cm^2 for the CR and RTR samples, respectively. The R_p value for the CR samples was 1.42 times that of the RTR samples. The R_p values of the CR and CR+ST(100 h) samples were higher than those of the RTR and RTR+ST(100 h) samples, respectively, which indicated that the CR Al−Mg−Mn−Sc alloy sheets have superior corrosion resistance. Faraday's law states that the corrosion rate (v) is positively related to corrosion current density (J_{corr}) [32]:

$$v=K\frac{J_{corr}N}{\rho} \tag{1}$$

where K is a constant of 3.27×10^{-3} mm·g/(μm·a); N is a constant related to the relative atomic mass of the materials; ρ is the density of the materials. Consequently, a decrease in the J_{corr} indicates an improvement in corrosion resistance. The J_{corr} recorded for the CR samples, being 7.03 μA/cm^2, was lower than 10.48 μA/cm^2 recorded for the RTR samples. The corrosion rates of the CR and RTR samples were determined to be 228 and 340 μm/a, respectively. The corrosion resistance decreased considerably after ST.

Figure 7(b) illustrates the Nyquist plots of different samples. Figure 7(c) depicts an enlarged image of the area highlighted in the red box in Fig. 7(b). The impedance values of the CR samples were the greatest, followed by the RTR samples. In contrast, the impedance values of the ST samples were reduced by an order of magnitude. Figure 7(d) depicts the Bode plots, which illustrates the relationship between the absolute impedance $|Z|$ and the phase angle as the frequency varies. The CR samples displayed the greatest absolute impedance $|Z|$ in the low-frequency range (<1 Hz). Remarkably, the absolute impedance $|Z|$ decreased significantly after ST, with the CR+ST(48 h) samples showing greater values in comparison to the RTR+ST(48 h) samples. The Nyquist curves were fitted according to the equivalent circuits depicted in Fig. 7(b). The fitting results were shown as the black dashed lines in Figs. 7(b) and (c). A constant phase element (CPE) was employed instead of a conventional capacitor. The electrolyte resistance of the solution is denoted as R_s. The charge transfer reactions on the alloy surface are represented by R_f and CPE_0. The R_f reflects the Faraday charge transfer resistance, which is proportional to the surface passive film. The fitting results are presented in Table 3, where n_1 is the exponent of CPE and is used to describe the capacitance characteristics of the electrochemical interface. The R_s remained stable across all samples. The R_f values of the rolled samples were higher than those of the ST samples. Specifically, the CR samples exhibited the highest R_f value of 52.00 kΩ·cm^2, which was more than twice as large as the value of RTR samples. The R_f value of the RTR+ST(100 h) samples was only 2.32 kΩ·cm^2.

Table 2 Fitting parameters of polarization curves

Sample	J_{corr}/ (μA·cm^{-2})	β_a/ (V·dec^{-1})	β_c/ (V·dec^{-1})	φ_{corr}(vs SCE)/ V	φ_{pit}(vs SCE)/ V	R_p/ (kΩ·cm^2)	Corrosion rate/ (μm·a^{-1})
CR	7.03	0.326	−0.156	−0.751	−0.197	6.52	228
RTR	10.48	0.343	−0.164	−0.839	−0.301	4.60	340
CR+ST(48 h)	25.10	0.382	−0.177	−0.836	−0.287	2.10	815
RTR+ST(48 h)	27.13	0.330	−0.239	−1.071	−0.618	2.22	881
CR+ST(100 h)	10.69	0.327	−0.168	−0.877	−0.414	4.51	347
RTR+ST(100 h)	12.88	0.258	−0.135	−0.928	−0.646	2.99	418

Table 3 Electrochemical parameters obtained by fitting EIS results

Sample	R_s/ ($\Omega\cdot cm^2$)	CPE_0/ ($\mu F\cdot cm^{-2}$)	n_1	R_f/ ($k\Omega\cdot cm^2$)
CR	24.70	5.6	0.90	52.00
RTR	23.30	7.5	0.95	23.50
CR+ST(48 h)	22.50	15.7	0.91	7.00
RTR+ST(48 h)	23.90	19.9	0.89	3.97
CR+ST(100 h)	21.70	12.5	0.92	3.72
RTR+ST(100 h)	19.70	19.0	0.83	2.32

4 Discussion

The IGC immersion tests, NAMLT tests, potentiodynamic polarization test, and EIS tests are reliable techniques for assessing the corrosion resistance of Al alloy. The results showed that pitting corrosion and IGC are two common corrosion types. In this work, the CR Al−Mg−Mn−Sc alloy sheets demonstrated superior corrosion resistance. In contrast, the corrosion current density of CR samples in the present study (7.03 μA/cm^2) was significantly lower than that of the AA5052 plates treated with micro-arc oxidation (32.5 μA/cm^2) [33]. Furthermore, the maximum IGC depth in the Al−Mg−Mn−Sc−Zr alloy prepared by the selective laser melting plus annealing at 598 K for 4 h was 46.76 μm [14]. QIU et al [33] reported a maximum corrosion depth of 69 μm for friction stir welded Al−4.5Mg−0.3Mn−0.1Sc−0.1Zr sheets. The above maximum corrosion depth is higher than the results in this work. In addition, there is a significant difference in φ_{corr} between different samples in this work, indicating that the rolling temperature affects the corrosion properties. The corrosion potentials of forged AA5080 alloy before and after annealing were −890.5 and −891.3 mV, respectively [34]. SINGH et al [27] reported that the φ_{corr} of CR AA5083 remained at −0.879 V after annealing at 573 K for 5 min. PAN et al [16] added Zn and Sc elements in Al−Mg alloy and the φ_{corr} of the alloy was less than −1.2 V. The φ_{corr} of CR samples in this work was higher than the above results. The improvement of CR on the corrosion properties of the Al−Mg−Mn−Sc alloy was discussed from the perspectives of passivation film, pitting, and IGC.

4.1 Effect of CR on passive film

The stable passive film could inhibit both pitting corrosion and IGC. The pitting resistance of Al alloys is greatly affected by the passive films, especially in terms of their hydration level and porosity [35]. Prior studies [36,37] have revealed that Mn can substantially enhance the corrosion resistance of Al alloy. The selective dissolution of Mn is believed to augment the free space at the metal/oxide interface, thereby facilitating the formation of a denser passive film.

The potentiodynamic polarization curves (Fig. 7(a)) revealed evident passivation behavior in all samples, except for RTR+ST(48 h) and RTR+ST(100 h). In terms of EIS results, a lower CPE_0 value indicates an increased difficulty in the penetration of water molecules, oxygen, and chloride ions, which reduces their absorption on the surface. Table 3 reveals that both CR and RTR samples exhibited lower CPE_0, indicating lower porosity and better uniformity of the passive film. The CR samples had the lowest CPE_0 compared to the other samples, therefore providing further evidence of their superior passive film and corrosion resistance. The R_f value decreased significantly after ST, suggesting an augmentation in the contact area between the electrolytes and the samples. Additionally, there was an infiltration of water molecules and oxygen ions on the surface, leading to the activation of the corrosion process [38]. The EIS results revealed that the R_f value of RTR samples is only 45.2% that of CR samples. The R_f of both CR and RTR samples decreased after ST, however, the R_f of the CR+ST samples remained higher than that of the RTR+ST samples under the same treatment conditions. This result indicates that the charge transfer layer passivation was improved upon the CR processing. Furthermore, Fig. 7(d) indicated that the phase angle peak was the widest for the CR samples, and narrower for the RTR and ST samples. A broader phase angle peak indicates a more stable protective barrier across a wider range of frequencies [39]. The protection frequency domain of the CR samples was wider, which ultimately led to better corrosion resistance. Notably, the correlation between the corrosion resistance and grain size conformed to the Hall−Petch relationship [40]. The non-equilibrium grain boundaries resulting from the fine grains led to an increased number of nucleation sites for the formation of a denser passive film [28]. In addition, the CR samples exhibited a finer grain structure, which formed thicker and more uniform passive films in comparison to the RTR

samples [41].

When Al alloys are immersed in NaCl solution, passive films are formed on their surfaces [14]. The thickness of the passive films (d) was estimated as follows [38,42]:

$$d=\frac{\varepsilon\varepsilon_0 A}{C} \tag{2}$$

where ε is the dielectric constant (relative electric permittivity) of barrier-type alumina (ε=20); ε_0 is the vacuum dielectric constant (ε_0=8.85×10^{-14} F/cm) [38,43]; A is the area of samples exposed to the solution (~1 cm^2); C is the capacitance from CPE_0. Hence, the calculated passive film thickness of CR samples is 3.16 nm, which is thicker than that of RTR samples (2.36 nm). After ST processing, the RTR+ST(100 h) sample had a passive film thickness of merely 0.89 nm, whereas the CR+ST(100 h) sample had a thickness of 1.41 nm. The thicker passive films on the CR samples are also reflected in the larger R_p and R_f values [42].

4.2 Effect of CR on pitting corrosion and IGC

Pitting corrosion in Al−Mg−Mn−Sc alloy is mainly caused by two microstructures: the coarsened Al_3(Sc,Zr) phase [43] and Al_6(Mn,Fe) phase. Sc element improves the corrosion resistance of the Al−Mg alloy [12]. The corrosion potential of the Al_3(Sc,Zr) phase is lower than that of the Al matrix, and Al_3(Sc,Zr) phase is found to be spontaneously passive with a low self-dissolution rate [32,44]. Furthermore, Al_3(Sc,Zr) phase, which exhibits coherence with the Al matrix, shows a high resistance to pitting corrosion. Nevertheless, the Sc and Zr atoms migrate short distances at high temperatures, leading to the coarsening of a few Al_3(Sc,Zr) phases and the formation of secondary Al_3(Sc,Zr) phases. Figures 4(a) and (b) depict the Al_3(Sc,Zr) phases in the CR and RTR samples, respectively. The Al_3(Sc,Zr) phases in the CR samples exhibited greater dispersal, thereby inhibiting the coarsening occurrence. Figure 8(a) shows the coarsened Al_3(Sc,Zr) phases in the RTR+A sample. The coarsened Al_3(Sc,Zr) phases then serve as a cathode, causing local corrosion of the surrounding Al matrix [14]. However, this kind of cathodic reaction is sluggish compared to the reactions of other intermetallic compounds. Therefore, the influence of the coarsened Al_3(Sc,Zr) phase on pitting corrosion is less than that of Al_6(Mn,Fe) secondary phase.

The Al_6(Mn,Fe) phase is the primary secondary phase in Al−Mg alloys and exhibits a lower corrosion potential than the Al matrix. Consequently, this phase serves as an anode in the corrosion system [44], causing localized corrosion in the exposed Al_6(Mn,Fe) phase. The size of the Al_6(Mn,Fe) phase is related to the pitting depth and area. Specifically, CR affects the size and distribution of the Al_6(Mn,Fe) phase significantly. The size of the Al_6(Mn,Fe) phase is shown in Figs. 8(b) and (c). The size of the Al_6(Mn,Fe) phase of the RTR samples was (343.2±157.8) nm, which was larger than that of the CR samples ((167.3±102.7) nm). The Al_6(Mn,Fe) phase in the CR samples was smaller than that in the RTR samples, aligning with the results of a prior investigation [20]. This was attributed to the fact that Al_6(Mn,Fe) phase exhibits brittleness at low-temperature and is prone to fracture under shear stress during the CR process [45]. Therefore, reducing the size of the Al_6(Mn,Fe) phase leads to smaller pits in the CR samples.

β phase in the Al−Mg alloy plays a crucial role in the IGC, and the distribution, size, and continuity of β phase impact corrosion resistance [13]. IGC initiation occurs resulting from the penetration of the Cl^- ion through the dense Al_2O_3 film [14]. Consequently, local microscopic inhomogeneity within the alloy creates an electrical potential difference, which leads to the second stage of pitting corrosion and IGC, in which the secondary and β phases serve as anodes. The rapid increase in IGC sensitivity growth is caused by the precipitation of β phase at the GBs. Figure 8(d) depicts the HRTEM image of β phase in the CR+ST sample. β phase was located near the GBs [46], corroborating the results illustrated in Fig. 4. The Al matrix on both sides of the GBs exhibited orientations along the [110] and [100] crystallographic directions. The following reactions occur during the IGC [12,28]:

$$Mg=Mg^{2+}+2e \tag{3}$$

$$Mg^{2+}+2H_2O=Mg(OH)_2+2H^+ \tag{4}$$

β phase dissolves in the IGC solution and forms active hydrides, resulting in the creation of high local hydrogen concentrations and fresh active surfaces near the GBs. This results in a continuous dissolution of β phase [28,47]:

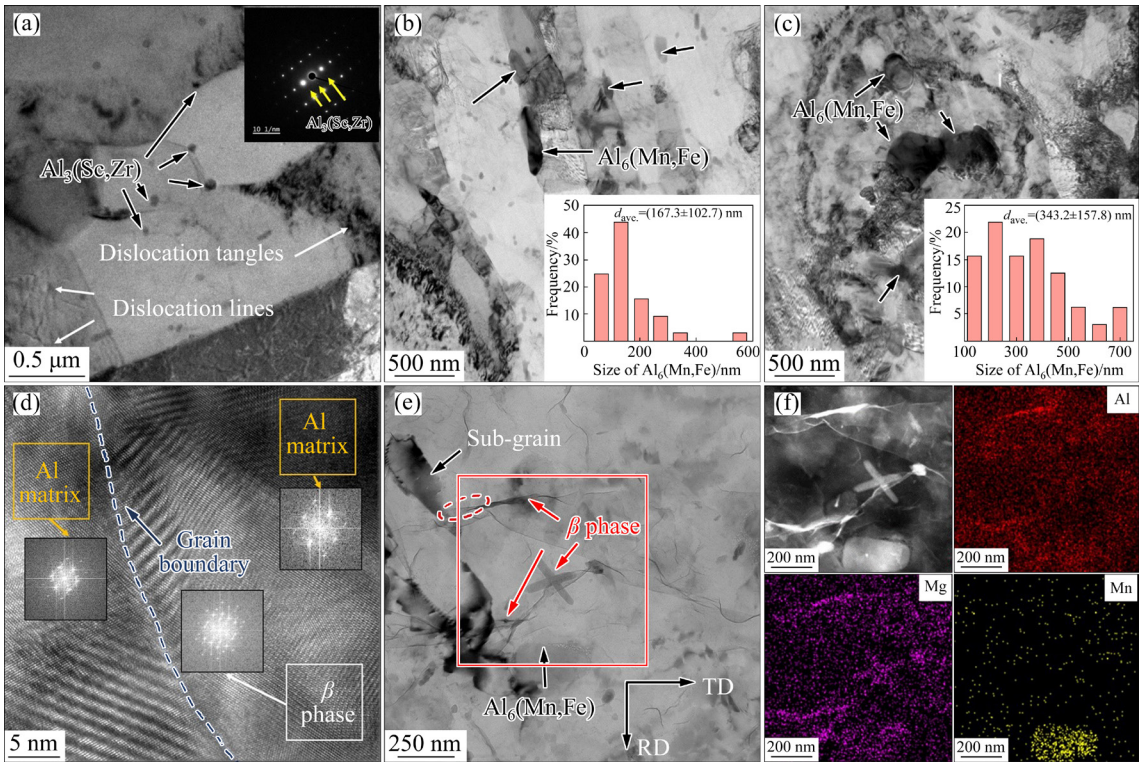

Fig. 8 TEM images of Al−Mg−Mn−Sc alloy sheets: (a) $Al_3(Sc,Zr)$ phases in RTR+A sample; (b, c) $Al_6(Mn,Fe)$ phases and phase sizes in CR and RTR samples, respectively; (d−f) β phase and its EDS mappings in CR+ST samples (The FFT patterns were generated from the regions indicated using orange boxes (Al matrix) and the white box (β phase))

$$Al_3Mg_2+13H^++13e=2MgH_2+3AlH_3 \quad (5)$$

$$MgH_2+2H_2O=Mg(OH)_2+2H_2 \quad (6)$$

Reactions (3)−(6) indicate that the rapid corrosion diffusion is closely related to the continuous distribution of β phase. To inhibit the spread of IGC, it is necessary to decrease the quantity of β phases and disperse the arrangement of β phase [2,6,11]. The addition of Mn in Al−Mg alloy can accelerate the uniform distribution of Mg within the Al matrix, thus inhibiting the formation of β phase in Al−Mg alloy [46,48]. GBs serve as nucleation sites for β phase, while the numerous vacancies in these GBs provide channels for the diffusion of Mg atoms [5,14]. Therefore, the nucleation, growth, and coarsening of β phase are more probable at GBs.

Numerous $Al_3(Sc,Zr)$ phases promoted heterogeneous nucleation during the casting process, resulting in the grain refinement and increased GBs [12,33], which lengthened the diffusion channel of the Mg element, thereby improving the corrosion resistance of Al−Mg−Mn−Sc alloys [49]. Fine and dispersed $Al_3(Sc,Zr)$ phases could pin at GBs and sub-GBs as well as induce the nucleation of β phase [28]. The uniform distribution of $Al_3(Sc,Zr)$ phases in the CR samples (Fig. 4(a)) induced a homogeneous dispersion of β phase in the Al matrix, thereby effectively preventing the formation of continuous β phases. As a result, the IGC sensitivity of the CR+ST samples was significantly reduced.

The misorientation of GBs exerts a significant impact on the formation of β phase corrosion resistance [8,9]. ORŁOWSKA et al [50] revealed that corrosion mainly occurs along high-energy interfaces, such as HAGBs. QIU et al [12] observed that β phase precipitates only along the GBs of recrystallized grains. The previous study [8] showed that HAGBs with higher energy promote the growth of β phase compared to LAGBs. An increase in the proportion of HAGBs increases the breadth of β phase. This phenomenon may be explained based on the GB precipitate growth theory [51,52]. A higher proportion of LAGBs leads to a reduced average width of GBs, which hinders the growth of β phase, the diffusion of the solute atoms inside the GBs, and the nucleation of β phase. CR induces more shear stress than RTR, resulting in

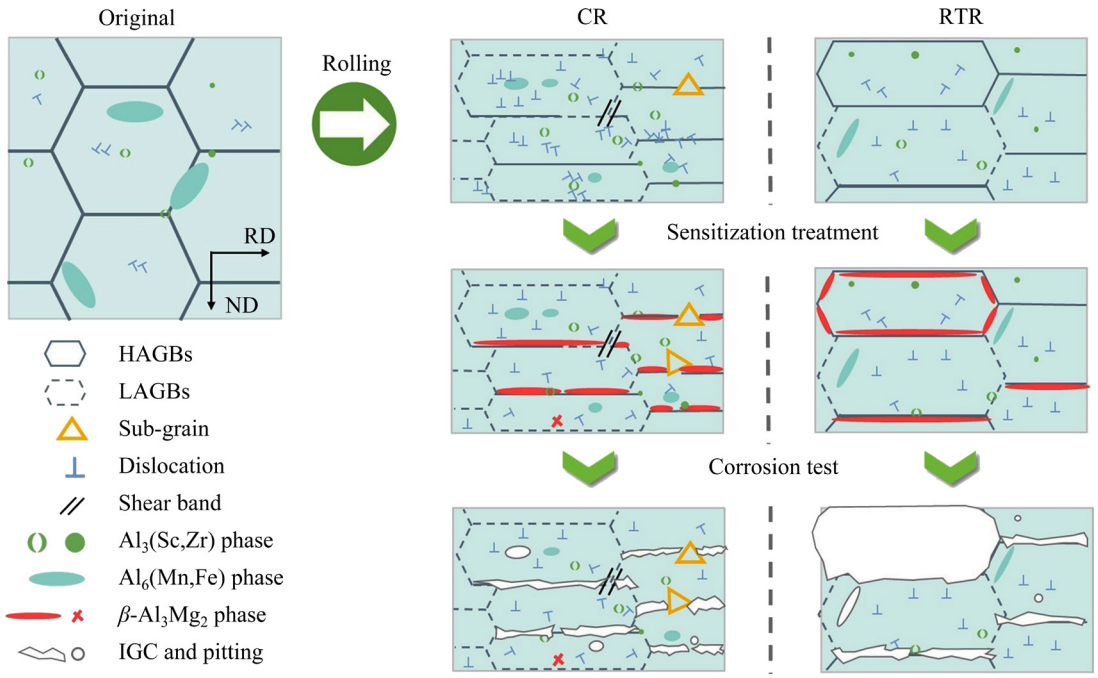

Fig. 9 Schematic diagrams of various microstructures and corresponding corrosion behaviors

a higher proportion of LAGBs. As depicted in Fig. 2, the proportion of HAGBs in the CR+A and RTR+A samples was 33.4% and 45.4%, respectively. The increased proportion of HAGBs facilitated the nucleation and growth of β phase during ST, leading to the heightened IGC sensitivity of these samples. The depiction of this mechanism is illustrated in Fig. 9.

Previous studies [12,53] suggested that the precipitation of β phase can be impeded by sub-grains. As depicted in Figs. 4(c) and (e), annealing and ST partially converted the high-density dislocations in the CR samples into sub-grains. These sub-grains hindered the precipitation of β phases (Fig. 4(e)). Furthermore, the shear bands obstructed the continuous precipitation of β phase. As seen in Fig. 4(e), β phase precipitated along the GBs, while its precipitation was significantly limited in the shear band region. As shown in Fig. 1, there are more shear bands in the CR samples due to extra shear stress. Figure 9 illustrates how shear bands and sub-grains hinder β precipitation effectively.

Besides GB diffusion, the dislocation pipe diffusion is another significant pathway for Mg atoms diffusion [7,11]. Figure 4 illustrates that the CR samples exhibit a higher density of dislocations compared to the RTR samples. This can be attributed to the inhibition of dynamic recovery during the deformation at low temperatures. However, the reduced proportion of HAGBs in the CR samples leads to difficulty in β phase nucleation at GBs. Numerous dislocations diffused the Mg atoms, leading to the formation of a fusiform β phase within the grains as depicted in Fig. 8(e) [4,7]. This phenomenon has not been reported in the existing literature. Since β phase within the grains is not continuous with β phase at GBs, the corrosion of β phase within the grain does not occur continuously. Thus, the IGC sensitivity is effectively reduced.

5 Conclusions

(1) The CR Al−Mg−Mn−Sc alloy showed superior corrosion resistance compared to the RTR samples. The maximum pitting depth of CR samples was only 9.8 μm. The pitting potential of the CR and RTR samples was −0.197 and −0.301 V, respectively. The IGC of Al−Mg−Mn−Sc alloy mostly occurs after ST. The CR+ST samples had the maximum corrosion depth of 35.2 μm, while the RTR+ST samples had a maximum corrosion depth of 53.9 μm. Notably, the former constituted just 65.3% of the latter. The DoS values were (56.89±2.52) and (73.11±2.63) mg/cm^2 for the CR+ST and RTR+ST samples, respectively.

(2) The CR Al−Mg−Mn−Sc alloy exhibits

enhanced corrosion resistance, due to the formation of thicker and more uniform passive films, which is facilitated by the finer grain structure and the beneficial role of manganese. The passive films of CR samples, with lower porosity and a broader protection frequency domain, provide a more stable barrier against pitting and IGC, as evidenced by the lower CPE_0 values and larger resistance values.

(3) The enhanced pitting corrosion resistance in the CR samples can be attributed to the thicker passivation film, the smaller size $Al_6(Mn,Fe)$ phase, and the even distribution of $Al_3(Sc,Zr)$ phase. Furthermore, the sub-grains and shear bands, together with a lower fraction of HAGBs in the CR samples effectively hindered the continuous precipitation of β phase at the grain boundaries, enhancing the IGC resistance of the CR samples. The undesirable precipitation of β phase in the CR samples was prevented, resulting in a significant reduction in the electrical coupling effects. The occurrence of pitting corrosion and IGC in CR samples is reduced.

CRediT authorship contribution statement

Hao GU: Experiments, Investigation, Writing – Original draft, Review & editing; **Shuai-guang JIA**, **Zhi-de LI**, **Hai-tao GAO** and **Zheng-yu WANG:** Investigation, Writing – Review & editing; **Charlie KONG:** Experiments, Investigation, Writing – Review & editing; **Hai-liang YU:** Conceptualization, Writing – Review & editing, Supervision, Project administration.

Declaration of competing interest

The authors declare that they have no known competing financial interests or personal relationships that could have appeared to influence the work reported in this paper.

Acknowledgments

The authors thank to the finial supports from the Project of the High-tech Industry Technology Innovation Leading Plan of Hunan Province, China (No. 2022GK4032) and the Innovation Driven Program of Central South University, China (No. 2019CX006). The authors also thank to Dr. Hui-jie CUI at Shimadzu (China) Co., Ltd., for the discussion of the results.

References

[1] BURGER G B, GUPTA A K, JEFFREY P W, LLOYD D J. Microstructural control of aluminum sheet used in automotive applications [J]. Materials Characterization, 1995, 35(1): 23−39.

[2] OGUOCHA I N A, ADIGUN O J, YANNACOPOULOS S. Effect of sensitization heat treatment on properties of Al−Mg alloy AA5083-H116 [J]. Journal of Materials Science, 2008, 43(12): 4208−4214.

[3] GUO Cheng, ZHANG Hai-tao, LI Shan-shan, CHEN Ri-xin, NAN Yun-fei, LI Lei, WANG Ping, LI Bao-mian, CUI Jian-zhong, NAGAUMI H. Evolution of microstructure, mechanical properties and corrosion behavior of Al−4Mg−2Zn−0.3Ag (wt.%) alloy processed by T6 or thermo-mechanical treatment [J]. Corrosion Science, 2021, 188: 109551.

[4] YANG Y K, ALLEN T. Direct visualization of β phase causing intergranular forms of corrosion in Al−Mg alloys [J]. Materials Characterization, 2013, 80: 76−85.

[5] TZENG Y C, CHEN R Y, LEE S L. Nondestructive tests on the effect of Mg content on the corrosion and mechanical properties of 5000 series aluminum alloys [J]. Materials Chemistry and Physics, 2021, 259: 124202.

[6] SCOTTO D'ANTUONO D, GAIES J, GOLUMBFSKIE W, TAHERI M L. Grain boundary misorientation dependence of β phase precipitation in an Al−Mg alloy [J]. Scripta Materialia, 2014, 76: 81−84.

[7] SCOTTO D'ANTUONO D, GAIES J, GOLUMBFSKIE W, TAHERI M L. Direct measurement of the effect of cold rolling on β phase precipitation kinetics in 5xxx series aluminum alloys [J]. Acta Materialia, 2017, 123: 264−271.

[8] ZHANG Rui-feng, QIU Yao, QI Yuan-shen, BIRBILIS N. A closer inspection of a grain boundary immune to intergranular corrosion in a sensitised Al−Mg alloy [J]. Corrosion Science, 2018, 133: 1−5.

[9] YAN Jian-feng, HODGE A M. Study of β precipitation and layer structure formation in Al 5083: The role of dispersoids and grain boundaries [J]. Journal of Alloys and Compounds, 2017, 703: 242−250.

[10] ZHU Ya-kun, CULLEN D A, KAR S, FREE M L, ALLARD L F. Evaluation of Al_3Mg_2 precipitates and Mn-rich phase in aluminum−magnesium alloy based on scanning transmission electron microscopy imaging [J]. Metallurgical and Materials Transactions A, 2012, 43(13): 4933−4939.

[11] GOSWAMI R, SPANOS G, PAO P S, HOLTZ R L. Precipitation behavior of the β phase in Al-5083 [J]. Materials Science and Engineering: A, 2010, 527(4/5): 1089−1095.

[12] QIU You-cai, YANG Xiao-fang, LI Jing-xiao, XIANG Shi-hua, SHI Jie, XU Jun-yao, SANDERS R E. The influence of Sc and Zr additions on microstructure and corrosion behavior of AA5182 alloy sheet [J]. Corrosion Science, 2022, 199: 110181.

[13] ZHANG R, ZHANG Y, YAN Y, THOMAS S, DAVIES C H J, BIRBILIS N. The effect of reversion heat treatment on the degree of sensitisation for aluminium alloy AA5083 [J]. Corrosion Science, 2017, 126: 324−333.

[14] ZHANG Han, GU Dong-dong, DAI Dong-hua, MA Cheng-long, LI Yu-xin, CAO Meng-zhen, LI Shu-hui. Influence of heat treatment on corrosion behavior of rare earth element Sc modified Al−Mg alloy processed by selective laser melting [J]. Applied Surface Science, 2020, 509: 145330.

[15] DENG Ying, ZHU Xin-wen, LAI Yi, GUO Yi-fan, FU Le,

XU Guo-fu, HUANG Ji-wu. Effects of Zr/(Sc+Zr) microalloying on dynamic recrystallization, dislocation density and hot workability of Al−Mg alloys during hot compression deformation [J]. Transactions of Nonferrous Metals Society of China, 2023, 33(3): 668−682.

[16] PAN Yan-lin, XU Yue, ZHANG Di, ZHANG Ji-shan, ZHOU Gu-xin, LANG Yu-jing. Mechanical properties, corrosion behavior and microstructure evolution of zinc and scandium co-strengthened 5xxx alloy [J]. Journal of Rare Earths, 2023, 41(11): 1819−1826.

[17] GAO Hai-tao, KONG C, YU Hai-liang. Lightweight metal laminated plates produced via (hot, cold and cryogenic) roll bonding: A review [J]. Transactions of Nonferrous Metals Society of China, 2023, 33(2): 337−356.

[18] GU Hao, LI Zhi-de, LIU Shi-lei, GAO Hai-tao, KONG C, YU Hai-liang. Asymmetric cryorolling and subsequent low-temperature annealing to improve mechanical properties of TA2 Ti sheets [J]. JOM, 2023, 75(8): 2865−2876.

[19] DU Qing-lin, LI Chang, CUI Xiao-hui, KONG C, YU Hai-liang. Fabrication of ultrafine-grained AA1060 sheets via accumulative roll bonding with subsequent cryorolling [J]. Transactions of Nonferrous Metals Society of China, 2021, 31(11): 3370−3379.

[20] GU Hao, BHATTA L, GAO Hai-tao, LI Zhi-de, KONG C, YU Hai-liang. Effect of cryorolling on the microstructure and high-temperature mechanical properties of AA5083 sheets [J]. Materials Science and Engineering A, 2022, 843: 143141.

[21] XIONG Han-qing, ZHOU Yu-exin, YANG Peng, KONG C, YU Hai-liang. Effects of cryorolling, room temperature rolling and aging treatment on mechanical and corrosion properties of 7050 aluminum alloy [J]. Materials Science and Engineering: A, 2022, 853: 143764.

[22] LI Chang, XIONG Han-qing, BHATTA L, WANG Lin, ZHANG Zhao-yang, WANG Hui, KONG C, YU Hai-liang. Microstructure evolution and mechanical properties of Al−3.6Cu−1Li alloy via cryorolling and aging [J]. Transactions of Nonferrous Metals Society of China, 2020, 30(11): 2904−2914.

[23] GU Hao, LI Zhi-de, LUO Kai-guang, BHATTA L, XIONG Han-qing, ZHANG Yun, KONG C, YU Hai-liang. Enhanced mechanical properties of AA5083 matrix composite via introducing Al0.5CoCrFeNi particles and cryorolling [J]. Acta Metallurgica Sinica (English Letters), 2022, 35(6): 879−889.

[24] KUMAR N, JAYAGANTHAN R, BROKMEIER H G. Effect of deformation temperature on precipitation, microstructural evolution, mechanical and corrosion behavior of 6082 Al alloy [J]. Transactions of Nonferrous Metals Society of China, 2017, 27(3): 475−492.

[25] GOPALA KRISHNA K, SIVAPRASAD K, SANKARA NARAYANAN T S N, HARI KUMAR K C. Localized corrosion of an ultrafine grained Al−4Zn−2Mg alloy produced by cryorolling [J]. Corrosion Science, 2012, 60: 82−89.

[26] LAXMAN MANI KANTA P, SRIVASTAVA V C, VENKATESWARLU K, PASWAN S, MAHATO B, DAS G, SIVAPRASAD K, KRISHNA K G. Corrosion behavior of ultrafine-grained AA2024 aluminum alloy produced by cryorolling [J]. International Journal of Minerals, Metallurgy, and Materials, 2017, 24(11): 1293−1305.

[27] SINGH D, RAO P N, RAJORIA C S, BHAMU J, GOEL S, RAYKAR S J, SAXENA K K, JAYAGANTHAN R. Influence of processing and microstructure on the corrosion behavior of ultrafine grained Al 5083 alloy [J]. Journal of Process Mechanical Engineering, 2024, 238(2): 533−543.

[28] TANG Zhong-qin, JIANG Feng, LONG Meng-jun, JIANG Jing-yu, LIU Hui-fang, TONG Meng-meng. Effect of annealing temperature on microstructure, mechanical properties and corrosion behavior of Al−Mg−Mn−Sc−Zr alloy [J]. Applied Surface Science, 2020, 514: 146081.

[29] FANG Hong-jie, LIU Hui, YAN Yang, LUO Xi-er, XU Xiang-chun, CHU Xin, LU Yu-jiao, YU Kun, WANG Dian-gang. Evolution of texture, microstructure, tensile strength and corrosion properties of annealed Al−Mg−Sc−Zr alloys [J]. Materials Science and Engineering: A, 2021, 804: 140682.

[30] DING Yu-sheng, WU Xiao-lan, GAO Kun-yuan, HUANG Cheng, XIONG Xiang-yuan, HUANG Hui, WEN Shen-ping, NIE Zuo-ren. The influence of stabilization treatment on long-term corrosion resistance and microstructure in Er and Zr containing 5083 aluminum alloy [J]. Materials Characterization, 2020, 161: 110143.

[31] ZHAO Y H, LIAO X Z, JIN Z, VALIEV R Z, ZHU Y T. Microstructures and mechanical properties of ultrafine grained 7075 Al alloy processed by ECAP and their evolutions during annealing [J]. Acta Materialia, 2004, 52(15): 4589−4599.

[32] SUNIL RAJ S, BLESSTO B, DHANASEKARAN S, SIVAPRASAD K, MUTHUPANDI V, SRIRAMANI N. Combination of high strength and corrosion resistance in AA5052 alloy using cryorolling and micro arc oxidation [J]. Materials Today: Proceedings, 2021, 39: 1738−1742.

[33] QIU You-cai, YANG Xiao-fang, XU Jun-yao, LI Jing-xiao, XIANG Shi-hua, CHEN Zhi-yu, SANDERS R E. Enhanced mechanical property and corrosion resistance of alloy 5182 FSW joints by Sc and Zr alloying [J]. Materials Characterization, 2022, 194: 112412.

[34] NEETU, SINGH S, RAO P N, JAYAGANATHAN R, MIDATHADA A, VERMA K, RAVELLA U K. Elevated corrosion in strain hardened Al−Mg alloy [J]. Vacuum, 2018, 157: 402−413.

[35] KAUFMAN J, RACEK J, CIESLAR M, MINÁRIK P, STEINER M A, MANNAVA S R, VASUDEVAN V K, SHARMA A, BÖHM M, BRAJER J, PILAŘ J, PÍNA L, MOCEK T. The effect of laser shock peening with and without protective coating on intergranular corrosion of sensitized AA5083 [J]. Corrosion Science, 2022, 194: 109925.

[36] CHEN Jia, XIAO Jian-wei, HUNG Chang-Yu, WANG Wen-bo, ZHAO Jing, MARC M F, DENG Chuang, CAI Wen-jun. Effects of alloying concentration on the aqueous corrosion and passivation of aluminum−manganese−molybdenum concentrated alloys [J]. Corrosion Science, 2022, 198: 110137.

[37] CHEN Jia, XIAO Jian-wei, POPLAWSKY J, MICHEL F M, DENG Chuang, CAI Wen-jun. The origin of passivity in aluminum-manganese solid solutions [J]. Corrosion Science, 2020, 173: 108749.

[38] BAJAT J B, MILOŠEV I, JOVANOVIĆ Z, JANČIĆ-HEINEMANN R M, DIMITRIJEVIĆ M, MIŠKOVIĆ-STANKOVIC V B. Corrosion protection of aluminium pretreated by vinyltriethoxysilane in sodium chloride solution [J]. Corrosion Science, 2010, 52(3): 1060−1069.

[39] TRDAN U, GRUM J. SEM/EDS characterization of laser

shock peening effect on localized corrosion of Al alloy in a near natural chloride environment [J]. Corrosion Science, 2014, 82: 328−338.
[40] RALSTON K D, BIRBILIS N, DAVIES C. H J. Revealing the relationship between grain size and corrosion rate of metals [J]. Scripta Materialia, 2010, 63(12): 1201−1204.
[41] DOLEGA Ł, ADAMCZYK-CIEŚLAK B, MIZERA J, KURZYDŁOWSKI K J. Corrosion resistance of model ultrafine-grained Al−Li alloys produced by severe plastic deformation [J]. Journal of Materials Science, 2012, 47(7): 3026−3033.
[42] GONZÁLEZ J A, LÓPEZ V, BAUTISTA A, OTERO E, NÓVOA X R. Characterization of porous aluminium oxide films from a.c. impedance measurements [J]. Journal of Applied Electrochemistry, 1999, 29(2): 229−238.
[43] WLOKA J, VIRTANEN S. Influence of scandium on the pitting behaviour of Al−Zn−Mg−Cu alloys [J]. Acta Materialia, 2007, 55(19): 6666−6672.
[44] CAVANAUGH M K, BIRBILIS N, BUCHHEIT R, BOVARD F G. Investigating localized corrosion susceptibility arising from Sc containing intermetallic Al_3Sc in high strength Al-alloys [J]. Scripta Materialia, 2007, 56(11): 995−998.
[45] YANG Bo-wei, GAO Min-qiang, LIU Yan, PAN Shuai, MENG Shuan-cheng, FU Ying, GUAN Ren-guo. Formation mechanism of refined Al_6(Mn,Fe) phase particles during continuous rheo-extrusion and its contribution to tensile properties in Al−Mg−Mn−Fe alloys [J]. Materials Science and Engineering: A, 2023, 872: 144952.
[46] ZHOU Deng-shan, ZHANG Xiu-zhen, TEHRANCHI A, HOU Jun-hua, LU Wen-jun, HICKEL T, PONGE D, RAABE D, ZHANG De-liang. Stacking faults in a mechanically strong Al(Mg)−Al_3Mg_2 composite [J]. Composites Part B: Engineering, 2022, 245: 110211.
[47] TRUEBA M, TRASATTI S P. The repassivation response from single cycle anodic polarization: The case study of a sensitized Al−Mg alloy [J]. Electrochimica Acta, 2018, 259: 492−499.
[48] MOFARREHI M, JAVIDANI M, CHEN X G. Effect of Mn content on the hot deformation behavior and microstructure evolution of Al−Mg−Mn 5xxx alloys [J]. Materials Science and Engineering: A, 2022, 845: 143217.
[49] GAO Yan, CHEN Wen-lin, GUO Zhen, WANG Liang. Effect of rare earth metals on mechanical and corrosion properties of Al−Zn−Mg−Cu−Zr alloy [J]. Rare Metal Materials and Engineering, 2017, 46(8): 2070−2075.
[50] ORŁOWSKA M, URA-BIŃCZYK E, OLEJNIK L, LEWANDOWSKA M. The effect of grain size and grain boundary misorientation on the corrosion resistance of commercially pure aluminium [J]. Corrosion Science, 2019, 148: 57−70.
[51] SPEIGHT M V. Growth kinetics of grain-boundary precipitates [J]. Acta Metallurgica, 1968, 16(1): 133−135.
[52] DING Qing-wei, ZHANG Di, ZUO Jin-rong, HOU Sheng-li, ZHUANG Lin-zhong, ZHANG Ji-shan. The effect of grain boundary character evolution on the intergranular corrosion behavior of advanced Al−Mg−3wt.%Zn alloy with Mg variation [J]. Materials Characterization, 2018, 146: 47−54.
[53] LI Zhao-ming, JIANG Hai-chang, WANG Yun-li, ZHANG Duo, YAN De-sheng, RONG Li-jian. Effect of minor Sc addition on microstructure and stress corrosion cracking behavior of medium strength Al−Zn−Mg alloy [J]. Journal of Materials Science & Technology, 2018, 34(7): 1172−1179.

深冷轧制在提高 Al−Mg−Mn−Sc 合金板材耐蚀性能中的作用

顾 昊[1,2]，贾帅广[1,2]，李智德[3]，高海涛[1,2,3]，王正宇[4]，Charlie KONG[5]，喻海良[1,2,3]

1. 中南大学 极端服役性能精密制造全国重点实验室，长沙 410083；
2. 中南大学 机电工程学院，长沙 410083；
3. 中南大学 轻合金研究院，长沙 410083；
4. 岛津(中国)有限公司，上海 200233；
5. Electron Microscope Unit, University of New South Wales, Sydney, NSW 2052, Australia

摘 要：通过调控轧制温度可以实现铝合金服役性能的提高。采用深冷轧制工艺提高了 Al−Mg−Mn−Sc 合金板材的耐蚀性能。相比室温轧制样品，深冷轧制压下量为 50%的样品表现出比室温轧制样品更好的耐蚀性能。经敏化处理后，深冷轧制样品的最大晶间腐蚀深度为 35.2 μm，而室温轧制样品的最大晶间腐蚀深度为 53.9 μm。同样，两个样品的质量损失分别为 56.89 和 73.11 mg/cm^2。此外，深冷样品的阻抗模量是室温轧制样品的 2 倍以上。深冷轧制样品中更厚的钝化膜，更细小分散的 Al_6(Mn,Fe)相使其具有更好的耐点蚀性能。深冷轧制样品中的亚晶粒、剪切带、分散的 Al_3(Sc,Zr)相、更少的大角度晶界和更高密度的位错均阻碍了 β (Al_3Mg_2)相在晶界的连续析出，同时促进 β 相在晶内形成，这些微观特征降低了 β 相与铝基体之间的电耦合效应，显著减少了晶间腐蚀的发生。

关键词：Al−Mg−Mn−Sc 合金；深冷轧制；耐蚀性能；显微组织；晶粒尺寸；第二相

(Edited by Wei-ping CHEN)